Revision 1

Word Count: 9239

Groundmass pyroxene crystal habits (trachts) record syneruptive magma dynamics in glassy pyroclasts

Names: Shota H. Okumura[1*], Satoshi Okumura[2], and Akira Miyake[1]

Affiliations:

[1]Department of Geology and Mineralogy, Division of Earth and Planetary Sciences,
Graduate School of Science, Kyoto University,
Kitashirakawaoiwake-cho, Sakyo-ku, Kyoto 606-8502, Japan

[2] Division of Earth and Planetary Materials Science, Department of Earth Science,
Graduate School of Science, Tohoku University,
6-3 Aoba, Aramaki-aza, Aoba, Sendai 980-8578, Japan

*Corresponding author: S.H. Okumura, okumura@kueps.kyoto-u.ac.jp

Abstract

Explosive eruptions produce various types of pyroclasts including those contain few with groundmass crystals. The textural variation such as the number density, size, and volume of groundmass crystals is expected to reveal the complex magma dynamics during syneruptive ascent in conduits; however, we have no quantitative method to investigate the magma dynamics based on crystal texture when the pyroclasts show glassy texture with a small number of microlites. Here we show that the variation of combination of crystallographic faces (i.e., tracht) of groundmass pyroxene crystals enables us to derive the degree of effective undercooling (ΔT_{eff}) and magma ascent histories even from the glassy pyroclasts. We conducted decompression experiments and analyzed trachts of groundmass pyroxene crystals in the run products in addition to those in natural pumices from the 1914 Plinian eruption of Sakurajima volcano. These results show that the glassy white pumices experienced higher ΔT_{eff} than the crystal-rich gray pumice, and corroborated that they originate from the magmas at different positions from the conduit walls. The estimate on ΔT_{eff} implies that the magma rapidly ascended in the center of the conduit might experience cooling because of volatile exsolution and expansion.

Keywords: pyroxene, crystal habit, crystal size distribution, nanolite, magma ascent

Introduction

Magma ascent histories in volcanic conduits are important for understanding the evolution of eruptive activities (Cashman and Sparks, 2013; Cassidy et al., 2018). The ascent histories can be recorded in the textures of groundmass crystals; therefore, the investigation of groundmass texture has played an important role to reveal the magma dynamics. Since the crystallization kinetics, especially nucleation rates, vary with the degree of effective undercooling (ΔT_{eff}) (e.g., Hammer and Rutherford, 2002; Brugger and Hammer, 2010; Shea and Hammer, 2013), the number density of groundmass crystals (Toramaru et al., 2008) and their size distribution (CSDs; Marsh, 1998) have been used to investigate magma ascent processes. These methods are based on the theoretical premise that the nucleation rate and the resultant number density are positively correlated with ΔT_{eff}. However, the positive correlation is not universally true. For instance, explosive eruptions can produce various types of pyroclasts, such as microlite-free white pumice with higher vesicularity and gray pumice with lower vesicularity and abundant microlites (e.g., Polacci, 2005). The glassy texture of the former is attributed to the considerably fast ascent; the ascending magma was probably quenched before crystallization could proceed to a significant extent or within the nucleation delay (e.g., Mollard et al., 2012; Arzilli et al., 2020; Rusiecka et al., 2020; Rusiecka and Martel, 2022). In this situation, it is difficult to extract syneruptive ascent histories from the crystal number densities in glassy pyroclasts, because the theoretical premise that the nucleation rate and the resultant number density are positively correlated with ΔT_{eff} is not valid. In such scenarios, a new indicator is required to estimate ΔT_{eff} from glassy groundmass with a small number of crystals.

Previous studies have demonstrated that crystal habits reflect ΔT_{eff} (e.g., Lofgren, 1974; Hammer and Rutherford, 2002; Shea and Hammer, 2013; Arzilli et al., 2022). Kouchi et al. (1983) revealed experimentally that the relative growth rates for different faces of clinopyroxene (Cpx) change with ΔT_{eff}. Their data indicates that, with increasing ΔT_{eff}, a pyroxene crystal would have different combinations of crystallographic faces (i.e., tracht; Sunagawa, 2005) by losing some faces. This hypothesis was confirmed by Okumura et al. (2022b), in which it was experimentally revealed that the tracht of groundmass pyroxene crystals changes from octagonal prisms consisting of {100}, {010}, and {110} prismatic faces into hexagonal prisms lacking {100} faces as ΔT_{eff} increases. Therefore, the tracht of groundmass pyroxene crystals is expected to allow us to estimate ΔT_{eff} and magma ascent histories from the glassy pyroclasts with a few number of the crystals.

In this study, we aim to infer magma ascent dynamics from the 1914 Sakurajima pumices including glassy one by the tracht analyses of groundmass pyroxene crystals. By performing decompression experiments on hydrous Sakurajima dacite magma, we investigated the differences in the syneruptive evolution of ΔT_{eff} and the magma ascent histories between the different pumice types. This study proposes the applicable analytical method to glassy pyroclasts towards the investigation of magma ascent dynamics during explosive eruptions.

Sample description

Sakurajima is located on the southern rim of the Aira caldera, Kyushu, Japan, with two summit vents aligned north–south: Kitadake and Minamidake. Eruptive activity has been summarized by Kobayashi et al. (2013) and is abridged here. Sakurajima started erupting at 26 ka, and its activity is subdivided into four stages based on tephra stratigraphy and chronology: the “Older Kitadake” (26–24 ka), “Younger Kitadake” (13–5 ka), “Older Minamidake” (4.5–1.6 ka), and “Younger Minamidake” (since 764 AD) stages. All eruptive products are andesitic to dacitic. Four large eruptions have occurred during the Younger Minamidake stage: the Tenpyo-Hoji (764–766), Bunmei (1471–1476), An-ei (1779–1782), and Taisho (1914–1915) eruptions. Each of these events had a similar eruptive sequence: an early Plinian eruption followed by lava outflows from lateral vents. In particular, the 1914–1915 Taisho eruption began with seismic activity on 11 January 1914, and the Plinian eruption began at the fissure vents on the western flank on 12 January; ten minutes later, a synchronous Plinian eruption began on the eastern flank. The Plinian phase continued on both flanks for about 36 h and was followed by lava extrusion and intermittent smaller explosions over the following two weeks. Additional outflows of lava began on the eastern flank in February and lasted for 1.5 years.

Seismic and geodetic monitoring of activity at Sakurajima has revealed the structure of the present magma plumbing system (e.g., Omori, 1916; Iguchi, 2013; Iguchi et al., 2013). A major magma reservoir exists at ~10 km depth beneath Aira caldera and minor reservoirs are present at ~5 km beneath the summit, from the north flank of Kitadake to Minamidake (Iguchi, 2013; Iguchi et al., 2013). The diameter of the conduit beneath Minamidake crater is estimated to be 300–500 m at 2 km depth and 40–60 m at the shallowest depths (Iguchi et al., 2013). Araya et al. (2019) analyzed melt inclusions in phenocrysts from the 1914 Sakurajima pumice and showed that the volatile saturation pressure ranged from 20 to 72 MPa. They proposed that the magma was pre-charged in a thick conduit at depths of 0.9–3.2 km below the surface, i.e., shallower than the minor reservoirs that feed present-day Vulcanian eruptions.

The textural analyses of the 1914 Sakurajima Plinian pumice have been performed by Nakamura (2006). The pumice clasts are classified into three types with different color, vesicularity, and microlite content. Type-1 and Type-2 are white pumice with high vesicularity (> 55 vol%): the former is glassy with lower modal abundance of plagioclase microlites than the latter (< 1.0 vs. 1.0–11.0 vol%). Type-3 is gray pumice with low vesicularity (25–50 vol%) and the relatively high modal abundance (8–16 vol%). All the types have similar bulk groundmass compositions (SiO_2 = 67–70 wt%) and the same mineral assemblage. Phenocrysts (> 100 μm in length) consist of plagioclase, orthopyroxene (Opx), augite, and magnetite, while microlites (< 100 μm) are plagioclase, Opx, pigeonite, augite, and titanomagnetite.

We collected pumice clasts erupted by the 1914 eruption from an outcrop at 4.5 km east of the Minamidake summit and examined three pumices as the representative of Type-1, 2, and 3.

Decompression experiments

We coarsely crushed the Type-1 pumice clasts, removed phenocrysts under an optical microscope, and collected the groundmass fragments as the starting material. Aliquots of 7–9 mg of the starting material and enough water (> 5 wt%) to achieve water-saturation were loaded into Au capsules (3 mm outer diameter and 1–2 cm long), sealed by welding. We conducted the experiments using the cold-seal pressure vessels with Ni filler rod at Tohoku University (Okumura et al., 2021). The decompression experiments were conducted in different manners: single step decompression (SSD) and continuous decompression (CD). The texture of SSD experiment shows the predominant crystal habits at a certain ΔT_{eff}, which allows us to investigate the relation between ΔT_{eff} and pyroxene crystal habits. By changing the degree of decompression, we can modulate the applied ΔT_{eff} during the SSD experiment. On the other hand, the CD experiment is an analogy for the actual ascent of magma, where the alleviation of ΔT_{eff} due to the crystallization can occur simultaneously with the increase in ΔT_{eff} induced by dehydration. The capsules were heated in the vessels at a temperature of 955 °C under a pressure of 120 MPa (assuming the minor reservoir at ~5 km depth) for 1 h and then isothermally decompressed to final pressures, P_{f}. In the SSD experiments, the capsule was rapidly decompressed (> 10 MPa/s) and held at P_{f} of 5, 10, 20, or 50 MPa for 3 h and then quenched by dropping it into a water-cooled zone in the system. The capsule in the CD experiment was decompressed to $P_{\mathrm{f}} = 5$ MPa with a rate of ~0.01 MPa/s and quenched immediately at P_{f} in the same way. Control experiments (EQ) were conducted by quenching without any decompression at temperatures of 935 or 955 °C to confirm the liquidus temperature at 120 MPa. The conditions and estimated ΔT_{eff} (discussed later) of experiments are listed in Table 1.

During the experiments, the oxygen fugacity (f_{O2}) was buffered at NNO to NNO+1 (Okumura et al., 2021). The error in temperature is assumed to be within ± 5 °C. Since the duration at the initial condition (955 °C) was restricted by the durability of pressure vessel, there is the possibility that the inherent heterogeneity of the starting material remains without equilibrium and affect the resultant textures of run products. For this reason, the error in ΔT_{eff} could be larger than the thermal error of ± 5 °C.

The recovered capsules were carefully opened; however, the recovered materials broke into pieces because of their high vesicularity and fragility, and lost their positional relations within the capsules. The materials were then mounted in resin for polishing and subsequent analyses.

Analytical methods

FE-SEM-EDS

The polished pumices and run products mounted in resin were observed using field-emission scanning electron microscopes (FE-SEMs) at Kyoto University. The chemical compositions of glasses were measured using a FE-SEM (JEOL JSM-7001F) coupled with an Oxford Instruments X-Max150 energy dispersive X-ray spectrometer (EDS) and its associated analytical software AZtec. The measurements were performed on multiple square regions (~1 × 1 μm^2) at an accelerating voltage of 15 kV and a beam current of about 0.10 nA for 60 s. Alkali (Na and K) losses during the measurements were corrected by calibration against analyses of larger areas in the sample or in closely relevant samples. The average glass compositions of pumices and run products are described in Table 2 and 3, respectively.

Textural analyses with SEM-BSE images

Backscattered electron (BSE) images for textural analyses of groundmass pyroxene crystals in samples and run products were obtained using a Thermo Fisher Scientific Helios NanoLab G3 CX FE-SEM operating at accelerating voltages of 5–10 kV and at working distances of 4–10 mm. In run products, 3–12 regions were selected for analysis in each sample and their BSE images were obtained at 3,500× magnification (corresponding to regions ~40–60 μm on a side and pixel sizes of ~20 nm). Using ImageJ software, we measured the areas of the rectangular regions examined (i.e., the entire image) and those occupied by vesicles and individual pyroxene cross sections, as well as pyroxene cross-sectional widths (w), which was measured as the minor axis of the best-fit ellipse. We discriminated pyroxene from other minerals based on their contrast in BSE images and SEM-EDS chemical maps. In addition, BSE images of pyroxene crystals larger than 0.2 μm wide were acquired at higher magnifications (10,000–65,000×) for tracht classification.

In the natural pumice samples, because of the low number densities of groundmass crystals, large rectangular areas were required to include a sufficient number of pyroxene crystals within the BSE images (e.g., >1 mm on a side for Type-1 pumice). However, it was difficult to acquire and process such a large image at a resolution adequate for the measurement of crystal size and tracht. Therefore, we obtained magnified images of the pyroxene crystals (magnifications of mainly 8,000–50,000× and pixel sizes of <20 nm) at an accelerating voltage of 5 kV and a working distance of 4 mm, as well as larger, lower-resolution (54 nm/pixel) BSE maps of the analyzed areas at an accelerating voltage of 10 kV and a working distance of 10 mm. The images of the analyzed areas were used to measure vesicularity and analyze the groundmass areas (i.e., excluding vesicles), and the magnified images were used to measure the sizes and trachts of groundmass pyroxene crystals in the same manner as in the run products. Analyzed crystals were larger than $10^{-0.8}$ μm (~0.16 μm) wide in accordance with the size interval of crystal size distributions (CSDs).

In BSE images at higher magnifications, each pyroxene cross section could be classified into one of several tracht types based on the number of faces between pairs of parallel faces: octagonal, heptagonal, hexagonal, pentagonal, or parallelogrammatic (Okumura et al. 2022b, 2023; Fig. 1). For example, the octagonal and hexagonal trachts have three and two faces between any pair of parallel faces, respectively, and the heptagonal tracht has the properties of the octagonal tracht on one side and those of the hexagonal tracht on the other (Fig. 1c). Pyroxene crystals that were difficult to classify as having a particular tracht were classified as “other”. If cross sections were incomplete (e.g., chipped), we classified them based on the remaining parts; however, those with no pairs of parallel faces were classified as “other” (Fig. 1d). Intermediate trachts, such as heptagonal, could only be identified when the cross section had almost all of the constituent faces (Fig.

1c). When multiple crystals were attached to each other, each individual crystal was classified separately (Fig. 1e).

Acquisition of tracht-specific CSDs

We acquired the size distributions of pyroxene cross sections in each tracht group (hereafter, tracht-specific CSDs). In run products, we counted the number of crystal cross sections of each tracht in each 0.4-μm size interval (i.e., 0.2–0.6 μm, 0.6–1.0 μm, etc.) and plotted the number at the center of the size interval. We did not calculate crystal number densities because the textures in the run products were extremely heterogeneous and thus could not be represented adequately by a single value.

For the natural pumice samples, the datasets of analyzed crystals were converted to tracht-specific CSDs using CSDCorrections v. 1.61 (Higgins, 2000), which converts cross-sectional widths into 3D long-axis lengths (L) using the 3D aspect ratio S:I:L (S and I being the short- and intermediate-axis lengths, respectively). We estimated the representative 3D aspect ratio of pyroxene crystals regardless of tracht for each sample by using ShapeCalc (Mangler et al., 2022), which compares a measured distribution of cross-sectional aspect ratios with model distributions based on the algorithm used in

CSDCorrections and returns estimated 3D aspect ratios (and the cumulative goodness of fit, R_c^2) for a range of shapes from 1:1:1 to 1:20:20. Although CSDCorrections yields 3D CSDs expressed as a function of L, we expressed the CSDs as a function of 3D short-axis lengths (S, or cross-sectional width) with additional corrections (i.e., S-plot CSDs; Okumura et al., 2022a). The details of the procedure for acquiring tracht-specific CSDs are described in Okumura et al. (2023). The CSDs were plotted in logarithmic size intervals with five intervals per decade larger than 0.1 μm (i.e., each interval is $10^{0.2}$ times as large as the next smaller interval: $10^{-1.0}$–$10^{-0.8}$ μm, $10^{-0.8}$–$10^{-0.6}$ μm, $10^{-0.6}$–$10^{-0.4}$ μm, etc.). We note that the effective image resolutions restricted our analysis to crystals larger than $10^{-0.8}$ μm.

TEM analyses

Groundmass pyroxene crystals in the samples were observed under a transmission electron microscope (TEM; JEOL, JEM-2100F) equipped with a Gatan Orius 200D CCD camera and a JEOL JET-2300T EDS detector at an accelerating voltage of 200 kV. Ultrathin sections approximately 100 nm thick were prepared using a focused ion beam system (Thermo Fisher Scientific, Helios NanoLab G3 CX): the Ga^+ ion gun was operated first at 30 kV and 21–0.083 nA, then at 16 kV and 0.13 nA for thinning, and finally at 2 kV and 77 pA for final processing. To determine mineral phases and crystallographic orientations, selected-area electron diffraction (SAED) patterns were analyzed using Gatan's proprietary DigitalMicrograph software and ReciPro (Seto and Ohtsuka, 2022). In addition, we obtained compositional maps of pyroxene crystals by EDS analyses in scanning TEM (STEM) mode. For quantitative X-ray analyses by STEM, we used the ζ-factor method (Watanabe and Williams, 2006). To achieve the accurate electron beam current measurements required for the ζ-factor method, appropriate calibration was performed with the CCD camera beforehand. Furthermore, we acquired annular dark-field STEM (ADF-STEM) images of pyroxene crystals perpendicular to their *c*-axes to observe compositional zoning at higher resolution.

Results

Textural variation of the Sakurajima pumice

Groundmass texture. As described in Nakamura (2006), groundmass crystals consisted of plagioclase, clinopyroxene (Cpx) including augite and pigeonite, orthopyroxene (Opx), and Fe-Ti oxide, with a trace amount of apatite. Their size range was mainly 0.1–10 μm in width.

Figure 2 shows the variation in groundmass texture among the pumice samples. The Type-1 pumice had higher vesicularity (75.0 %; Table 4), deformed vesicles, thinner vesicle walls, and few groundmass crystals (Fig. 2). The Type-2 pumice showed a vesicle texture similar to the Type-1 pumice but had more groundmass crystals and more-evolved glass composition (SiO_2 ~ 70 wt%, 1 % higher than Type-1; Table 2). The groundmass pyroxene crystals were characterized by hexagonal and parallelogrammatic trachts in the Type-1 and Type-2 white pumice samples (Fig. 2).

In contrast, the Type-3 pumice showed distinct textures (Fig. 2): lower vesicularity (67.1 %; Table 4), less-round vesicle shapes, thicker vesicle walls, abundant groundmass crystals, and the most evolved glass composition (SiO_2 ~ 73 wt%; Table 2). In addition, the groundmass crystals in the Type-3 pumice were loosely oriented (lateral direction in Fig. 2). The crystals were slightly rounded, and groundmass pyroxene crystals were characterized by rounded octagonal tracht.

Tracht-specific CSDs. Figure 3 shows the results of shape estimation by ShapeCalc. The best-estimated shape (*S*:*I*:*L*) was 1.00:1.40:3.60, 1.00:1.75.6.00, and 1.00:1.30:4.60 for the Type-1, Type-2, and Type-3 samples, respectively (Table 5). Note that the number of crystal cross sections used for the estimation (n = 90) was fewer than the recommended number (> 200; Mangler et al., 2022); therefore, the estimated 3D aspect ratio in the Type-1 pumice should involve large uncertainty, as shown in Figure 3a.

With the estimated 3D aspect ratios, the conventional (i.e., including all crystal trachts) and tracht-specific CSDs were acquired (Fig. 4). The conventional CSDs were concave up, especially in the white pumice samples (black lines in Fig. 4a and 4b). Their slopes were steepest at the size range of nanolite (i.e., crystals smaller than 1 μm in width; Mujin et al., 2017). In contrast, the conventional CSD in the Type-3 pumice (Fig. 4c) showed a gentler slope. The Type-3 pumice contained large crystals (mainly < 5 μm in width) as compared with the two white pumice samples. The crystal number density was the highest in the Type-3 pumice, and the lowest in the Type-1 pumice.

The tracht-specific CSDs exhibit an obvious difference between the white pumice (Type-1 and Type-2) and the gray pumice (Type-3). In the white pumice samples, octagonal pyroxene crystals had larger widths (mainly > 1 μm), and parallelogrammatic ones were distributed in the size range of nanolites (i.e., < 1 μm in width), where the conventional CSDs showed the steepest slope (Fig. 4a and 4b). Hexagonal crystals were distributed throughout the size range of both microlite and nanolite. The CSD slopes of these trachts were consistent with those of the conventional CSDs at the corresponding size ranges. Heptagonal and pentagonal trachts, which are the transient shapes between hexagonal and octagonal or parallelogrammatic trachts, exhibited the intermediate size ranges and slopes (Fig. 4b). In contrast, the tracht-specific CSD of the gray pumice sample (Type-3) was characterized by only the octagonal distribution with a gentle slope (Fig. 4c). Almost all of the nanolites showed octagonal tracht.

Internal texture of groundmass pyroxene crystals. The results of TEM observation are shown in Figures 5–7. The parallelogrammatic tracht consists of {110} prismatic faces (Fig. 6). The hexagonal tracht is composed of {110} and {010} faces (Fig. 5), and the octagonal tracht has additional {100} faces (Fig. 7). The mineral phases of groundmass pyroxene crystals were mainly Cpx composed of augite (*C*2/*c*) and pigeonite

($P2_1/c$) (Figs. 6 and 7), and occasionally Opx (Fig. 5). The Opx domain, when present, was distributed along (100) plane at the center of crystal (Fig. 5). The center of pyroxene crystals tended to be occupied by Ca-poor phases (i.e., pigeonite and Opx), and both sides were generally Cpx including augite (Figs. 5–7). Pigeonite domains showed anti-phase boundaries (Fig. 6h).

The pyroxene crystals sometimes showed concentric zonation. The pyroxene crystals tended to be Al-poor at their cores (Figs. 5c, 6c, and 7c); moreover, the Al content decreased again at their rims in those from the Type-3 pumice sample (Fig. 7c). In addition, the pyroxene crystals from the Type-3 sample showed normal zoning in Mg# [=Mg/(Mg + Fe) in mol; Fig. 7d]. We found an octagonal pyroxene microlite with parallelogrammatic zonation from the Type-3 pumice (Fig. 7).

Decompression experiments

The SEM and TEM analyses showed that the groundmass of the control experiment at 935 °C (EQ935°C120MPa1h) contained augite, low-Ca pyroxene (Opx and pigeonite), Fe-Ti oxides (magnetite and hematite), plagioclase, and apatite. Groundmass pyroxene crystals were mostly augite and ubiquitous in the groundmass (Fig. 8a and 8b). In contrast, the experiments at 955 °C showed inhomogeneous textures (Fig. 8c). The mineral assemblage in the control experiment at 955°C (EQ955°C120MPa1h) was augite, Fe-Ti oxides, and apatite; however, most of their groundmass rarely contained pyroxene crystals (Fig. 8c and 8d). The crystallization of Fe-Ti oxides occurred especially at the sample surfaces (i.e., near the capsule walls and vesicles), and pyroxene (augite) showed a similar tendency (Fig. 8c). The pyroxene crystallized locally, and their size and number density showed large variations among locations. The subsequent decompression induced crystallization of augite and plagioclase; however, the large part of groundmass remained glassy, which indicates that the decompression-induced crystallization in these experiments mainly occurred as heterogeneous nucleation on the pre-existing crystals and/or the sample surfaces. On the other hand, apatite crystals were distributed throughout the sample, and their size was generally a few hundred nanometers wide in all the run products.

Figures 9 and 10 show the BSE images of groundmass pyroxene crystals and the distributions of trachts for the experiments at 955 °C. The proportion of crystals in each tracht varied in association with the experimental conditions (Fig. 10; Table 6). At the initial condition (EQ955°C120MPa1h), the pyroxene trachts were mainly octagonal and hexagonal (Figs. 9a and 10a). Although the decompression to 50 MPa

(SSD955°C50MPa1h) resulted in the predominance of octagonal tracht (Figs. 9b and 10b), further decompression reproduced hexagonal and parallelogrammatic trachts. The texture at 20 MPa (SSD955°C20MPa1h) was characterized by all the types of tracht (Figs. 9c and 10c), and the proportion of hexagonal tracht increased at the expense of octagonal one at 10 MPa (SSD955°C10MPa1h; Figs. 9d and 10d). The texture of SSD955°C5MPa1h was characterized by parallelogrammatic tracht (Figs. 9e and 10e). We did not confirm obvious correlation between tracht and local number densities in these runs. The CD experiment (CD955°C5MPa3h) was characterized by octagonal and hexagonal trachts (Figs. 9f and 10f). In the CD experiment, the crystals tended to be hexagonal and parallelogrammatic in the regions where their number density was relatively low, although the proportion of parallelogrammatic crystals was still low. Note that the TEM analyses confirmed that each type of tracht comprises the same prismatic faces as those observed in the pumice samples.

Discussion

Estimating the pyroxene liquidus for the Sakurajima melt

Estimation of the value of ΔT_{eff} for each experiment required the pyroxene liquidus in the Sakurajima melt. In our experiments at 955 °C, most parts of the groundmass were glassy (Fig. 8d).

Because superliquidus heating hinders subsequent crystal nucleation (e.g., Sato, 1995; Pupier et al., 2008; Waters et al., 2015; Arzilli et al., 2015; First et al., 2020; Matsumoto et al., 2023), this result indicates that the pyroxene crystals and any crystal nuclei were dissolved in the melt at the initial conditions (i.e., 120 MPa and 955 °C), and that the liquidus temperature of Cpx in this composition at 120 MPa is below 955 °C. In contrast, the control experiment at 935 °C contained ubiquitous groundmass pyroxene (Fig. 8b). Therefore, the Cpx liquidus temperature at 120 MPa must be within the range 935–955 °C in our experiments.

In contrast, Sekine et al. (1979) estimated pyroxene and plagioclase liquidi by performing phase equilibrium experiments on the groundmass of the pumice from the 1914 Sakurajima eruption under water-saturated conditions at the NNO buffer. Their result at 100 MPa shows that the liquidus temperature of Cpx is below 930 °C, whereas our results show that the liquidus temperature of Cpx is within 935–955 °C at 120 MPa. This difference can be attributed to the Mg content of the melt. The MgO content of the groundmass glass in the Sakurajima pumice used by Sekine et al. (1979; 0.75 wt%) is lower than that in our experiments (around 1.0 wt%; Tables 2 and 3), a discrepancy also reported by Nakamura (2006). Therefore, we thermodynamically modeled the effect of MgO content on the Cpx liquidus using MELTS (Ghiorso and Sack, 1995; Gualda et al., 2012; Ghiorso and Gualda, 2015). We used rhyolite-MELTS in MELTS_Excel (Gualda and Ghiorso, 2015) and obtained pyroxene liquidus curves for two melt compositions: the starting materials in our experiments and those used by Sekine et al. (1979) (Fig. 11). This calculation showed that increasing the MgO content of the melt by ~0.3 wt% from that used by Sekine et al. (1979) raises the liquidus temperature by ~25 °C. Additionally, the experimental liquidus can be reproduced by adding 55 °C to the calculated liquidus (Fig. 11).

Magma ascent process deduced from white pumice

As reported by Nakamura (2006), the white pumice samples, especially Type-1, were characterized by the low crystal number density (Fig. 4a). Assuming that the pyroxene crystals in the Type-1 pumice crystallized under higher ΔT_{eff}, their shapes might be more elongated than those in other pumice samples (e.g., Kouchi et al., 1983; Shea and Hammer, 2013). On the contrary, the Type-1 pumice had the lowest degree of pyroxene elongation (i.e., *L*/*S* ratio) of the three samples (Table 5). This might be attributed to the estimation uncertainty due to the insufficient number of analyzed crystals (< 200; Mangler et al., 2022). Although an underestimated value of 3D aspect ratio can affect resultant CSDs, the crystal number density is still the lowest in the Type-1 pumice. When using the 3D aspect ratio of

1.00:1.40:10.00 instead of the estimated value (1.00:1.40:3.60), the population densities (*N*) decrease by approximately one natural log unit in the *S*-plot CSD (Fig. 4), and the CSD shapes are largely maintained. Therefore, the uncertainty in 3D aspect ratio has negligible impact on the following discussion.

The crystallization experiments demonstrated that Cpx tracht changes with the extent of decompression (Fig. 10). Based on the liquidus curve (Fig. 11), the estimated ΔT_{eff} at 955 °C was approximately 35, 75, 95, and 110 °C at 50, 20, 10, and 5 MPa, respectively. Therefore, our results indicate that the Cpx tracht changes from octagonal to hexagonal and then to parallelogrammatic with increasing ΔT_{eff} (Fig. 10). As shown in the tracht-specific CSDs (Fig. 4a and 4b), the tracht of groundmass pyroxene crystals in the white pumice samples (Type-1 and 2) changes from octagonal to parallelogrammatic with decreasing size. Assuming that smaller crystals were crystallized at shallower part in the conduit, the tracht-specific CSDs indicate that pyroxene crystallization in the white pumice samples changed from octagon- and hexagon-dominant to hexagon- and parallelogram-dominant during syneruptive ascent (Fig. 4a and 4b). Our experimental results (Fig. 10) imply that the magma that produced the white pumice experienced increasing ΔT_{eff} due to accelerated ascent in the conduit. The concave-up shapes of the conventional CSDs (Fig. 4a and 4b) consistently show the accelerated nucleation of crystals, indicating the increase of ΔT_{eff} (e.g., Armienti et al., 1994; Marsh, 1998; Armienti, 2008). This inference is also supported by the Al-increasing zonation (Fig. 5c and 6c) because the enrichment of pyroxene in Al indicates rapid growth (e.g., Dymek and Gromet, 1984; Mollo et al., 2013; Masotta et al., 2020). Therefore, we conclude that the magma that produced the white pumices ascended sufficiently fast and reached the surface before crystallization could proceed to a significant extent, attaining a high ΔT_{eff}.

The minimum decompression rate of the white pumice magma can be constrained from our CD experiment. Decompression at a constant rate of ~0.01 MPa/s mainly produced octagonal and hexagonal Cpx crystals (Fig. 10f), whereas rapid decompression in a single step (> 10 MPa/s) mainly produced parallelogrammatic crystals (Fig. 10e). Therefore, ascent must have been faster than 0.01 MPa/s, which is plausible when compared with rates estimated for Vulcanian eruptions: 0.28–0.87 × 10^{-2} MPa/s for the 1975–1987 eruptions by Miwa et al. (2009; based on the microlite number density water exsolution rate meter developed by Toramaru et al., 2008); 0.7–7.8 × 10^{-2} MPa/s for the 2010 eruption by Miwa and Geshi (2012; based on cracked texture of microphenocrysts).

Because plagioclase and Cpx are the main phenocryst phases in the natural pumices (Nakamura, 2006), the crossing of their liquidi should indicate the magma storage conditions prior to the 1914 Sakurajima eruption. Our Cpx liquidus crosses that of plagioclase from Sekine et al. (1979) around 50 MPa and 990 °C (Fig. 11), consistent with previous estimates of the storage pressure (20–72 MPa based on the water contents of phenocryst-hosted melt inclusions; Araya et al., 2019) and temperature (940–1010 °C based on the pyroxene thermometry; Matsumoto and Nakamura, 2017). Given that the pumices were quenched at ~5 MPa, based on the water content in the groundmass (ca. 0.4 wt%; Nakamura, 2006), decompression from 50 MPa yields $\Delta T_{\mathrm{eff}} \approx 75$ °C under water-saturated conditions. On the other hand, the similarity in tracht proportions (Figs. 4 and 10) indicates that the maximum ΔT_{eff} attained during ascent was probably between 70 and 110 °C, which appears to be higher than the estimation based on melt dehydration alone ($\Delta T_{\mathrm{eff}} \approx 75$ °C). Therefore, the parallelogrammatic tracht common in the white pumices probably resulted from the adiabatic cooling associated with volatile exsolution and expansion (Mastin and Ghiorso, 2001; La Spina et al., 2015; Arzilli et al., 2019). Microlite crystallization may also release latent heat (e.g., Couch et al., 2003b; Blundy et al., 2006; La Spina et al., 2015), but this is unlikely given the low degree of crystallization.

Implication

The tracht-specific CSD of the gray pumice sloped gently and was dominated by octagonal pyroxene crystals spanning a broader size distribution than pyroxene crystals in the white pumices (Fig. 4c), indicating relatively prolonged crystallization under lower ΔT_{eff}. The decrease in Al content with growth (Fig. 7c) supports the slow or declining growth. In addition, the slightly rounded shapes of the groundmass crystals (Figs. 2 and 7) suggest resorption by heating. We also observed a Cpx microlite with parallelogrammatic zoning, implying that this crystal nucleated under high ΔT_{eff}. These textures indicate that the gray pumice magma initially nucleated microlites under high ΔT_{eff} before prolonged crystallization under decreasing ΔT_{eff}, and that the magma temperature surpassed the pyroxene liquidus just before quenching.

Assuming that the gray pumice originated from portions of the ascending magma nearer to the conduit walls (Nakamura, 2006), two sources of heat are plausible: the release of latent heat by crystallization (Couch et al., 2003a; Blundy et al., 2006) and shear heating (Mastin, 2005; Costa et al., 2007; Hale et al., 2007). Since the crystallization increases magma temperature by 2.3–3.2 °C per 1 % (Couch et al., 2003a; Blundy et al., 2006), the temperature rise by the latent heat release can be up to 50 °C by assuming 15 %

crystallization of pyroxene + plagioclase (Table 4; Nakamura, 2006). Moreover, shear heating can increase magma temperature by several tens of degrees (e.g., Mastin, 2005; Costa et al., 2007; Hale et al., 2007). The weak orientation of the groundmass crystals (Fig. 2) suggests shear deformation. Furthermore, shear heating is enhanced in the presence of crystals (Mueller et al., 2010). Therefore, both heating processes were probably significant during groundmass crystallization in the gray pumice, resulting in the rounding of the groundmass crystals.

Finally, the textural differences between the white and gray pumices indicate that they probably originated from the same magma but different radial positions within the conduit (e.g., Polacci, 2005; Nakamura, 2006): the white pumice represents magma that ascended rapidly in the center of the conduit, whereas the gray pumice originated from magma nearer the conduit walls (Fig. 12). Magma flows more slowly in the vicinity of the conduit walls than in the center of the conduit because of wall-generated friction (e.g., Gonnermann and Manga, 2003; Mastin, 2005; Costa et al., 2007; Hale and Mühlhaus, 2007). The low vesicularity of gray pumice is attributed to the efficient degassing near the walls due to the longer duration for gas escape and the shear deformation (e.g., Stasiuk et al., 1996; Okumura et al., 2009, 2013). The shear deformation also facilitates crystallization (e.g., Kouchi et al., 1986; Kolzenburg et al., 2018; Vetere et al., 2021), favoring the nucleation of groundmass crystals.

Our investigation demonstrates the value of pyroxene tracht analyses for unraveling magma ascent dynamics via the evolution of ΔT_{eff}. Because this method is applicable to crystal-poor glassy samples and achieves high temporal resolution when crystals are zoned, further such tracht analyses should contribute to a better understanding of syneruptive magma ascent dynamics.

Acknowledgments

We thank K. Matsumoto and M. Mujin for their help with sample collection at Sakurajima. This study was supported by the Fukada Grant-in-Aid from the Fukada Geological Institute and JST SPRING (Grant Number JPMJSP2110) to SO and JSPS KAKENHI Grant Number JP20H00198, JP20H00205, and JP21H01182 to AM. This study was supported by the Integrated Program for Next Generation Volcano Research and Human Resource Development by MEXT (Grant Number JPJ005391).

References

Araya, N., Nakamura, M., Yasuda, A., Okumura, S., Sato, T., Iguchi, M., Miki, D., and Geshi, N. (2019) Shallow magma pre-charge during repeated Plinian eruptions at Sakurajima volcano. Scientific reports, 9, 1979. https://doi.org/10.1038/s41598-019-38494-x

Armienti, P. (2008) Decryption of Igneous Rock Textures: Crystal Size Distribution Tools. Reviews in Mineralogy and Geochemistry, 69, 623–649. https://doi.org/10.2138/rmg.2008.69.16

Armienti, P., Pareschi, M.T., Innocenti, F., and Pompilio, M. (1994) Effects of magma storage and ascent on the kinetics of crystal growth. Contributions to Mineralogy and Petrology, 115, 402–414. https://doi.org/10.1007/BF00320974

Arzilli, F., Agostini, C., Landi, P., Fortunati, A., Mancini, L., and Carroll, M.R. (2015) Plagioclase nucleation and growth kinetics in a hydrous basaltic melt by decompression experiments. Contributions to Mineralogy and Petrology, 170, 55. https://doi.org/10.1007/s00410-015-1205-9

Arzilli, F., La Spina, G., Burton, M.R., Polacci, M., Le Gall, N., Hartley, M.E., Di Genova, D., Cai, B., Vo, N.T., Bamber, E.C., and others. (2019) Magma fragmentation in highly explosive basaltic eruptions induced by rapid crystallization. Nature Geoscience, 12, 1023–1028. https://doi.org/10.1038/s41561-019-0468-6

Arzilli, F., Stabile, P., Fabbrizio, A., Landi, P., Scaillet, B., Paris, E., and Carroll, M.R. (2020) Crystallization kinetics of alkali feldspar in peralkaline rhyolitic melts: implications for Pantelleria volcano. Frontiers in Earth Science, 8, 177.

https://doi.org/10.3389/feart.2020.00177

Arzilli, F., Polacci, M., La Spina, G., Le Gall, N., Llewellin, E.W., Brooker, R.A., Torres-Orozco, R., Di Genova, D., Neave, D.A., Hartley, M.E., and others. (2022) Dendritic crystallization in hydrous basaltic magmas controls magma mobility within the Earth's crust. Nature Communications, 13, 3354. https://doi.org/10.1038/s41467-022-30890-8

Blundy, J., Cashman, K., and Humphreys, M. (2006) Magma heating by decompression-driven crystallization beneath andesite volcanoes. Nature, 443, 76–80. https://doi.org/10.1038/nature05100

Brugger, C.R., and Hammer, J.E. (2010) Crystallization kinetics in continuous decompression experiments: implications for interpreting natural magma ascent processes. Journal of Petrology, 51, 1941–1965. https://doi.org/10.1093/petrology/egq044

Cashman, K.V., and Sparks, R.S.J. (2013) How volcanoes work: A 25 year perspective. GSA Bulletin, 125, 664–690. https://doi.org/10.1130/B30720.1.

Cassidy, M., Manga, M., Cashman, K., and Bachmann, O. (2018) Controls on explosive-effusive volcanic eruption styles. Nature communications, 9, 2839. https://doi.org/10.1038/s41467-018-05293-3

Costa, A., Melnik, O., and Vedeneeva, E. (2007) Thermal effects during magma ascent in conduits. Journal of Geophysical Research: Solid Earth, 112, B12205. https://doi.org/10.1029/2007JB004985

Couch, S., Harford, C.L., Sparks, R.S.J., and Carroll, M.R. (2003a) Experimental constraints on the conditions of formation of highly calcic plagioclase microlites at the Soufrire Hills Volcano, Montserrat. Journal of Petrology, 44, 1455–1475. https://doi.org/10.1093/petrology/44.8.1455

Couch, S., Sparks, R.S.J., and Carroll, M.R. (2003b) The kinetics of degassing-induced crystallization at Soufriere Hills Volcano, Montserrat. Journal of Petrology, 44, 1477–1502. https://doi.org/10.1093/petrology/44.8.1477

Dymek, R.F., and Gromet, L.P. (1984) Nature and origin of orthopyroxene megacrysts from the St-Urbain anorthosite massif, Quebec. The Canadian Mineralogist, 22, 297–326.

First, E.C., Leonhardi, T.C., and Hammer, J.E. (2020) Effects of superheating magnitude on olivine growth. Contributions to Mineralogy and Petrology, 175, 13. https://doi.org/10.1007/s00410-019-1638-7

Ghiorso, M.S., and Sack, R.O. (1995) Chemical mass transfer in magmatic processes IV. A revised and internally consistent thermodynamic model for the interpolation and extrapolation of liquid-solid equilibria in magmatic systems at elevated temperatures and pressures. Contributions to Mineralogy and Petrology, 119, 197–212. https://doi.org/10.1007/BF00307281

Ghiorso, M.S., and Gualda, G.A.R. (2015) An H2O–CO2 mixed fluid saturation model compatible with rhyolite-MELTS. Contributions to Mineralogy and Petrology, 169, 53. https://doi.org/10.1007/s00410-015-1141-8

Gonnermann, H.M., and Manga, M. (2003) Explosive volcanism may not be an inevitable consequence of magma fragmentation. Nature, 426, 432–435.

https://doi.org/10.1038/nature02138

Gualda, G.A.R., and Ghiorso, M.S. (2015) MELTS_Excel: A Microsoft Excel-based MELTS interface for research and teaching of magma properties and evolution. Geochemistry, Geophysics, Geosystems, 16, 315–324. https://doi.org/10.1002/2014GC005545

Gualda, G.A.R., Ghiorso, M.S., Lemons, R.V., and Carley, T.L. (2012) Rhyolite-MELTS: a modified calibration of MELTS optimized for silica-rich, fluid-bearing magmatic systems. Journal of Petrology, 53, 875–890. https://doi.org/10.1093/petrology/egr080

Hale, A.J., and Mühlhaus, H.B. (2007) Modelling shear bands in a volcanic conduit: implications for over-pressures and extrusion-rates. Earth and Planetary Science Letters, 263, 74–87. https://doi.org/10.1016/j.epsl.2007.08.026

Hale, A. J., Wadge, G., and Mühlhaus, H.B. (2007) The influence of viscous and latent heating on crystal-rich magma flow in a conduit. Geophysical Journal International, 171, 1406–1429. https://doi.org/10.1111/j.1365-246X.2007.03593.x

Hammer, J.E., and Rutherford, M.J. (2002) An experimental study of the kinetics of decompression-induced crystallization in silicic melt. Journal of Geophysical Research, 107, 1–24. https://doi.org/10.1029/2001JB000281

Higgins, M.D. (2000) Measurement of crystal size distributions. American Mineralogist, 85, 1105–1116. https://doi.org/10.2138/am-2000-8-901

Iguchi, M. (2013) Magma Movement from the Deep to Shallow Sakurajima Volcano as Revealed by Geophysical Observations. Bulletin of the Volcanological Society of

Japan, 58, 1–18. https://doi.org/10.18940/kazan.58.1_1

Iguchi, M., Tameguri, T., Ohta, Y., Ueki, S., and Nakao, S. (2013) Characteristics of Volcanic Activity at Sakurajima Volcano's Showa Crater During the Period 2006 to 2011. Bulletin of the Volcanological Society of Japan, 58, 115–135. https://doi.org/10.18940/kazan.58.1_115

Kobayashi, T., Miki, D., Sasaki, H., Iguchi, M., Yamamoto, T., and Uto, K. (2013) Geological Map of Sakurajima Volcano (2nd edition). Geological Survey of Japan (In Japanese with English abstract).

Kolzenburg, S., Giordano, D., Hess, K.U., and Dingwell, D.B. (2018) Shear rate-dependent disequilibrium rheology and dynamics of basalt solidification. Geophysical Research Letters, 45, 6466–6475. https://doi.org/10.1029/2018GL077799

Kouchi, A., Sugawara, Y., Kashima, K., and Sunagawa, I. (1983) Laboratory growth of sector zoned clinopyroxenes in the system CaMgSi2O6–CaTiAl2O6. Contributions to Mineralogy and Petrology, 83, 177–184. https://doi.org/10.1007/BF00373091

La Spina, G., Burton, M., and Vitturi, M.D.M. (2015) Temperature evolution during magma ascent in basaltic effusive eruptions: A numerical application to Stromboli volcano. Earth and Planetary Science Letters, 426, 89–100. https://doi.org/10.1016/j.epsl.2015.06.015

Lofgren, G. (1974) An experimental study of plagioclase crystal morphology; isothermal crystallization. American Journal of Science, 274, 243–273.

Mangler, M.F., Humphreys, M., Wadsworth, F.B., Iveson, A.A., and Higgins, M.D. (2022)

Variation of plagioclase shape with size in intermediate magmas: a window into incipient plagioclase crystallisation. Contributions to Mineralogy and Petrology, 177, 64. https://doi.org/10.1007/s00410-022-01922-9

Marsh, B.D. (1998) On the interpretation of crystal size distributions in magmatic systems. Journal of Petrology, 39, 553–599. https://doi.org/10.1093/petroj/39.4.553

Masotta, M., Pontesilli, A., Mollo, S., Armienti, P., Ubide, T., Nazzari, M., and Scarlato, P. (2020) The role of undercooling during clinopyroxene growth in trachybasaltic magmas: Insights on magma decompression and cooling at Mt. Etna volcano. Geochimica et Cosmochimica Acta, 268, 258–276. https://doi.org/10.1016/j.gca.2019.10.009

Mastin, L.G. (2005) The controlling effect of viscous dissipation on magma flow in silicic conduits. Journal of Volcanology and Geothermal Research, 143, 17–28. https://doi.org/10.1016/j.jvolgeores.2004.09.008

Mastin, L.G., and Ghiorso, M.S. (2001) Adiabatic temperature changes of magma–gas mixtures during ascent and eruption. Contributions to Mineralogy and Petrology, 141, 307–321. https://doi.org/10.1007/s004100000210

Matsumoto, K., and Nakamura, M. (2017) Syn-eruptive breakdown of pyrrhotite: a record of magma fragmentation, air entrainment, and oxidation. Contributions to Mineralogy and Petrology, 172, 83. https://doi.org/10.1007/s00410-017-1403-8

Matsumoto, K., Okumura, S., and Tomiya, A. (2023) Effect of pre-existing crystals and melt homogeneity on the decompression-induced crystallization of hydrous rhyodacite magma. American Mineralogist, in press. https://doi.org/10.2138/am-2022-8723

Miwa, T., and Geshi, N. (2012) Decompression rate of magma at fragmentation: Inference from broken crystals in pumice of vulcanian eruption. Journal of Volcanology and Geothermal Research, 227, 76–84. https://doi.org/10.1016/j.jvolgeores.2012.03.003

Miwa, T., Toramaru, A., and Iguchi, M. (2009) Correlations of volcanic ash texture with explosion earthquakes from vulcanian eruptions at Sakurajima volcano, Japan. Journal of Volcanology and Geothermal Research, 184, 473–486. https://doi.org/10.1016/j.jvolgeores.2009.05.012

Mollard, E., Martel, C. and Bourdier, J.L. (2012) Decompression-induced crystallization in hydrated silica-rich melts: empirical models of experimental plagioclase nucleation and growth kinetics. Journal of Petrology, 53, 1743–1766.

Mollo, S., Blundy, J.D., Iezzi, G., Scarlato, P., and Langone, A. (2013) The partitioning of trace elements between clinopyroxene and trachybasaltic melt during rapid cooling and crystal growth. Contributions to Mineralogy and Petrology, 166, 1633–1654. https://doi.org/10.1007/s00410-013-0946-6

Mueller, S., Llewellin, E.W., and Mader, H.M. (2010) The rheology of suspensions of solid particles. Proceedings of the Royal Society A: Mathematical, Physical and Engineering Sciences, 466, 1201–1228. https://doi.org/10.1098/rspa.2009.0445

Mujin, M., Nakamura, M., and Miyake, A. (2017) Eruption style and crystal size distributions: Crystallization of groundmass nanolites in the 2011 Shinmoedake eruption. American Mineralogist, 102, 2367–2380. https://doi.org/10.2138/am-2017-6052CCBYNCND

Nakamura, K. (2006) Textures of plagioclase microlite and vesicles within volcanic products of the 1914-1915 eruption of Sakurajima Volcano, Kyushu, Japan. Journal of Mineralogical and Petrological Sciences, 101, 178–198.

Okumura, S., Nakamura, M., Takeuchi, S., Tsuchiyama, A., Nakano, T., and Uesugi, K. (2009) Magma deformation may induce non-explosive volcanism via degassing through bubble networks. Earth and Planetary Science Letters, 281, 267–274. https://doi.org/10.1016/j.epsl.2009.02.036

Okumura, S., Nakamura, M., Uesugi, K., Nakano, T., and Fujioka, T. (2013) Coupled effect of magma degassing and rheology on silicic volcanism. Earth and Planetary Science Letters, 362, 163–170. https://doi.org/10.1016/j.epsl.2012.11.056

Okumura, S., Ishibashi, H., Itoh, S., Suzumura, A., Furukawa, Y., Miwa, T., and Kagi, H. (2021) Decompression experiments for sulfur-bearing hydrous rhyolite magma: Redox evolution during magma decompression. American Mineralogist, 106, 216–225. https://doi.org/10.2138/am-2020-7535

Okumura, S.H., Mujin, M., Tsuchiyama, A., and Miyake, A. (2022a) 3D crystal size distributions of pyroxene nanolites from nano X-ray computed tomography: Improved correction of crystal size distributions from CSDCorrections for magma ascent dynamics in conduits. American Mineralogist, 107, 1766–1778. https://doi.org/10.2138/am-2022-8039

Okumura, S.H., Okumura, S., and Miyake, A. (2022b) Tracht change of groundmass pyroxene crystals in decompression experiments. Journal of Mineralogical and Petrological Sciences, 117, 211219. https://doi.org/10.2465/jmps.211219

Okumura, S.H., Mujin, M., Tsuchiyama, A., and Miyake, A. (2023) Crystal habit (tracht) of groundmass pyroxene crystals recorded magma ascent paths during the 2011 Shinmoedake eruption. American Mineralogist, in press. https://doi.org/10.2138/am-2022-8765

Omori, F. (1916) The Sakura-jima eruption and earthquakes II. Bulletin of The Imperial Earthquake Investigation Committee, 8, 35–179.

Polacci, M. (2005) Constraining the dynamics of volcanic eruptions by characterization of pumice textures. Annals of Geophysics, 48, 731–738. http://hdl.handle.net/2122/934

Pupier, E., Duchene, S., and Toplis, M.J. (2008) Experimental quantification of plagioclase crystal size distribution during cooling of a basaltic liquid. Contributions to Mineralogy and Petrology, 155, 555–570. https://doi.org/10.1007/s00410-007-0258-9

Rusiecka, M.K., and Martel, C. (2022) Nucleation delay in water-saturated rhyolite during decompression in shallow volcanic systems and its implications for ascent dynamics. Bulletin of Volcanology, 84, 61. https://doi.org/10.1007/s00445-022-01569-1

Rusiecka, M.K., Bilodeau, M., and Baker, D.R. (2020) Quantification of nucleation delay in magmatic systems: experimental and theoretical approach. Contributions to Mineralogy and Petrology, 175, 47. https://doi.org/10.1007/s00410-020-01682-4

Sato, H. (1995) Textural difference between pahoehoe and aa lavas of Izu-Oshima volcano, Japan—an experimental study on population density of plagioclase. Journal of Volcanology and Geothermal Research, 66, 101–113. https://doi.org/10.1016/0377-0273(94)00055-L

Sekine, T., Katsura, T. and Aramaki, S. (1979) Water saturated phase relations of some andesites with application to the estimation of the initial temperature and water pressure at the time of eruption. Geochimica et Cosmochimica Acta, 43, 1367–1376.

Seto, Y., and Ohtsuka, M. (2022) ReciPro: free and open-source multipurpose crystallographic software integrating a crystal model database and viewer, diffraction and microscopy simulators, and diffraction data analysis tools. Journal of Applied Crystallography, 55, 397–410. https://doi.org/10.1107/S1600576722000139

Shea, T., and Hammer, J.E. (2013) Kinetics of cooling- and decompression-induced crystallization in hydrous mafic-intermediate magmas. Journal of Volcanology and Geothermal research, 260, 127–145. https://doi.org/10.1016/j.jvolgeores.2013.04.018

Stasiuk, M.V., Barclay, J., Carroll, M.R., Jaupart, C., Ratté, J.C., Sparks, R.S.J., and Tait, S.R. (1996) Degassing during magma ascent in the Mule Creek vent (USA). Bulletin of Volcanology, 58, 117–130. https://doi.org/10.1007/s004450050130

Sunagawa, I. (2005) Crystals: Growth, Morphology, and Perfection, 295 p. Cambridge

University Press, New York.

Toramaru, A., Noguchi, S., Oyoshihara, S., and Tsune, A. (2008) MND(microlite number density) water exsolution rate meter. Journal of Volcanology and Geothermal Research, 175, 156–167. https://doi.org/10.1016/j.jvolgeores.2008.03.035

Vetere, F., Petrelli, M., Perugini, D., Haselbach, S., Morgavi, D., Pisello, A., Iezzi, G., and Holtz, F. (2021) Rheological evolution of eruptible Basaltic-Andesite Magmas under dynamic conditions: The importance of plagioclase growth rates. Journal of Volcanology and Geothermal Research, 420, 107411. https://doi.org/10.1016/j.jvolgeores.2021.107411

Watanabe, M., and Williams, D.B. (2006) The quantitative analysis of thin specimens: a review of progress from the Cliff-Lorimer to the new z-factor methods. Journal of microscopy, 221, 89–109. https://doi.org/10.1111/j.1365-2818.2006.01549.x

Waters, L.E., Andrews, B.J., and Lange, R.A. (2015) Rapid crystallization of plagioclase phenocrysts in silicic melts during fluid-saturated ascent: phase equilibrium and decompression experiments. Journal of Petrology, 56, 981–1006. https://doi.org/10.1093/petrology/egv025

Zingg, T. (1935) Beitrag zur Schotteranalyse. Schweizerische Mineralogische und Petrographische Mitteilungen, 15, 39–140 (in German).

Figure captions

Figure 1. Classification of pyroxene trachts. (**a**) A 3D shape of pyroxene crystal with octagonal tracht. (**b**) The shape variation of cross section depending on trachts. (**c**) Cross sections of groundmass pyroxene crystals were classified based on the number of faces between a given pair of parallel faces (indicated by circles). (**d**) Incomplete shapes were classified similarly if a pair of parallel faces was present. (**e**) Individual segments of attached crystals were classified in a similar manner.

Figure 2. BSE images of groundmass of the Sakurajima pumice samples. Groundmass crystal phases are Fe-Ti oxides, pyroxene, and plagioclase (in order of decreasing brightness). The brightness of the groundmass glass is similar to that of plagioclase. Black regions are vesicles. The images in the right column show the groundmass pyroxene crystals with trachts characteristic of each sample. Abbreviations: Pl = plagioclase; Px = pyroxene; Ox = Fe-Ti oxides.

Figure 3. Estimation of 3D aspect ratio of groundmass pyroxene crystals by ShapeCalc

(Mangler et al., 2022). The best-fitted 300 estimates are plotted in Zingg diagram (Zingg, 1935) with the colors based on the cumulative goodness of fit (R_c^2). The uncertainties (1σ) on the best shape estimate are provided as black bars. Note that the plotted distributions do not necessarily represent the actual variation of crystal shapes: we did not find tabular cross sections of pyroxene through the SEM observation, but most pyroxene crystals seemed to have acicular shapes in 3D as far as we observed. Abbreviations: S = short-axis length, I = intermediate-axis length, L = long-axis length.

Figure 4. Tracht-specific CSDs of groundmass pyroxene crystals in the Sakurajima pumice samples. The conventional CSDs (i.e., including all trachts) are plotted in black for comparison. The size range shown is from 0.16 to 6.31 μm in width (short-axis length). The total number of analyzed crystals and the proportions of crystals in each tracht are shown at top-right in each panel.

Figure 5. Internal texture of a hexagonal pyroxene nanolite in the Type-1 pumice. (**a**) An ADF-STEM image, (**b**–**d**) Ca, Al, and Mg# (=Mg/(Mg + Fe) in mol) compositional maps, respectively, and (**e**) a SAED pattern were obtained along the [001] zone axis. (**f** and

g) SAED patterns were obtained from the points 1 and 2 in (**a**), at another orientation. (**g**) The SAED pattern from Cpx region showed weak reflections of $P2_1/c$ in addition to those of $C2/c$ (i.e., the hkl reflections of "$h + k$ = even"). Abbreviations: Opx, orthopyroxene; Cpx, clinopyroxene.

Figure 6. Internal texture of a parallelogrammatic clinopyroxene nanolite in the Type-2 pumice.

(**a**) An ADF-STEM image, (**b**–**d**) Ca, Al, and Mg# compositional maps, respectively, and (**e**) a SAED pattern were obtained along the [001] zone axis. SAED patterns were also obtained at another orientation from (**f**) the center and (**g**) the left side of the crystal. There are weak reflections of $P2_1/c$ in (**g**). (**h**) A dark-field image with reflection $\boldsymbol{g} = 0\bar{3}\bar{1}$ shows anti-phase boundaries in the pigeonite (Pgt) domain.

Figure 7. Internal texture of an octagonal clinopyroxene microlite in the Type-3 pumice.

(**a**) An ADF-STEM image and (**b**–**d**) Ca, Al, and Mg# compositional maps, respectively, were obtained along the [001] zone axis. Note that the Al-rich spot within the crystal is groundmass glass. There is a parallelogrammatic zonation inside the rounded octagonal outline.

Figure 8. Backscattered electron (BSE) images of control experiments at 120 MPa. The run products at 935 °C (EQ935°C120MPa1h; **a** and **b**) and 955 °C (EQ955°C120MPa1h; **c** and **d**). The control experiment at 955 °C resulted in inhomogeneous texture: Fe-Ti oxides and pyroxene crystallized locally near the sample surface (upper-left part in **c**) whereas most of the groundmass was glassy (**d**). Abbreviations: Px, pyroxene; Ox, Fe-Ti oxides; Pl, plagioclase.

Figure 9. BSE images of groundmass pyroxene crystals in run products at 955 °C. The control experiment at 120 MPa (**a**; EQ955°C120MPa1h). The single-step decompression experiments at the final pressure of 50 (**b**; SSD955°C50MPa3h), 20 (**c**; SSD955°C20MPa3h), 10 (**d**; SSD955°C10MPa3h), and 5 MPa (**e**; SSD955°C5MPa3h). The continuous decompression experiment from 120 to 5 MPa (**f**; CD955°C5MPa3h). Abbreviations: Px, pyroxene; Ap, apatite.

Figure 10. Tracht-specific CSDs of pyroxene crystals produced in experiments at 955 °C.

(**a**) EQ955°C120MPa1h, (**b**) SSD955°C50MPa3h, (**c**) SSD955°C20MPa3h, (**d**) SSD955°C10MPa3h, (**e**) SSD955°C5MPa3h, and (**f**) CD955°C5MPa3h. The number of crystal sections (*n*) is plotted on a logarithmic scale against cross-sectional width for each size interval. The size range shown is from 0.20 to 4.20 μm in width. The total number of analyzed crystals and the proportions of crystals in each tracht are shown at top-right in each panel.

Figure 11. Estimated magma storage conditions and liquidus curves for the 1914 Sakurajima magma. Cpx (black), Opx (gray), and plagioclase liquidi (blue) reported by Sekine et al. (1979) are shown alongside pyroxene liquidi for the melt compositions of Sekine et al. (1979; yellow) and this study (red) modeled using MELTS. The calculated curves were shifted by 55 °C from the MELTS calculations to match the experimental results. A black horizontal bar represents the range of possible Cpx liquidus temperatures constrained by the control experiments in this study (i.e., 935–955 °C). The shaded area indicates the magma storage conditions estimated based on pyroxene thermometry (Matsumoto and Nakamura, 2017) and phenocryst-hosted melt inclusion H_2O contents (Araya et al., 2019).

Figure 12. Syneruptive magma ascent dynamics in the conduit. (**a**) Schematic illustration of the horizontal variation of magma ascent in conduit. (**b** and **c**) Qualitative illustration of ΔT_{eff} evolution for the gray and white pumice magmas. The magma that ascended rapidly in the center of the conduit originated the white pumice, whereas the magma that ascended in the vicinity of the conduit walls produced the gray pumice. Dashed lines in (**a**) are the isochronal contours of ascending magma at t_0–t_3. White circles and black objects represent vesicles and groundmass pyroxene crystals, respectively. The magmatic processes which increase or decrease ΔT_{eff} are written in blue or red characters, respectively. After the nucleation delay ($t > t_2$), pyroxene nucleation occurred under high ΔT_{eff}. Then, the white pumice magma was quenched, whereas the gray pumice magma experienced prolonged crystallization under the ΔT_{eff} lowered by heating processes (i.e., the release of latent heat of crystallization and the shear heating).

Tables

Table 1. The experimental conditions and resultant textures.

Name	T (°C)	Path	P_i (MPa)	P_f (MPa)	duration (h)	GM phase [a]	ΔT_{eff} for Px (K)	Main Px tracht
EQ935C120MPa1h	935	EQ	120	120	1	Px, Pl, Ox, Ap	10	8, 6
EQ955C120MPa1h	955	EQ	120	120	1	Px, Ox, Ap	~0	8, 6
SSD955C50MPa3h	955	SSD	120	50	3	Px, Pl, Ox, Ap	35	8
SSD955C20MPa3h	955	SSD	120	20	3	Px, Pl, Ox, Ap	75	8, 6, 4
SSD955C10MPa3h	955	SSD	120	10	3	Px, Pl, Ox, Ap	95	6
SSD955C5MPa3h	955	SSD	120	5	3	Px, Pl, Ox, Ap	110	4
CD955C5MPa3h	955	CD	120	5	3	Px, Pl, Ox, Ap	<110	8, 6

[a] Abbreviation: Px, pyroxene; Pl, plagioclase; Ox, Fe-Ti oxide; Ap, apatite.

Table 2. Average glass compositions of Sakurajima pumices.

	Type-1		Type-2		Type-3	
(wt%)	n = 98		n = 55		n = 41	
SiO_2	68.80	(0.27)	70.01	(0.31)	73.41	(0.24)
TiO_2	0.80	(0.07)	0.78	(0.08)	0.90	(0.06)
Al_2O_3	13.94	(0.13)	13.64	(0.15)	11.84	(0.14)
FeO	4.62	(0.19)	4.29	(0.14)	4.08	(0.16)
MnO	0.11	(0.12)	0.10	(0.12)	0.04	(0.09)
MgO	1.07	(0.05)	0.89	(0.06)	0.48	(0.07)
CaO	3.70	(0.14)	3.34	(0.14)	1.96	(0.06)
Na_2O	4.35	(0.12)	4.25	(0.14)	3.90	(0.11)
K_2O	2.44	(0.07)	2.57	(0.07)	3.19	(0.07)
P_2O_5	0.17	(0.11)	0.13	(0.12)	0.21	(0.11)
Total	100		100		100	

NOTES: Values in parentheses are standard deviations.

Oxide concentrations were recalculated to total 100% by cation balance.

Table 3. Average glass compositions of run products.

(wt%)[a]	Starting material n = 45	EQ955°C 120MPa1h n = 39	EQ945°C 120MPa1h n = 30	EQ935°C 120MPa1h n = 29	SSD955°C 50MPa3h n = 33	SSD955°C 20MPa3h n = 37	SSD955°C 10MPa3h n = 40	SSD955°C 5MPa3h n = 45	CD955°C 5MPa3h n = 36
SiO_2	68.99 (0.23)	71.06 (0.42)	71.22 (0.38)	70.58 (0.51)	70.35 (0.32)	71.18 (0.49)	70.96 (0.39)	71.47 (0.40)	70.86 (0.39)
TiO_2	0.79 (0.08)	0.73 (0.10)	0.74 (0.11)	0.73 (0.15)	0.67 (0.07)	0.66 (0.14)	0.64 (0.15)	0.64 (0.11)	0.61 (0.08)
Al_2O_3	13.91 (0.11)	14.43 (0.13)	14.42 (0.11)	14.23 (0.14)	14.3 (0.11)	14.49 (0.13)	14.5 (0.15)	14.59 (0.13)	14.42 (0.12)
FeO	4.47 (0.14)	2.15 (0.19)	2.07 (0.16)	3.24 (0.42)	3.33 (0.13)	2.08 (0.48)	2.27 (0.24)	1.79 (0.19)	2.76 (0.15)
MnO	0.07 (0.11)	0.06 (0.10)	0.1 (0.11)	0.09 (0.12)	0.07 (0.11)	0.11 (0.12)	0.06 (0.10)	0.05 (0.09)	0.10 (0.12)
MgO	1.05 (0.05)	0.89 (0.10)	0.92 (0.07)	0.93 (0.07)	0.91 (0.09)	0.87 (0.17)	0.85 (0.18)	0.84 (0.17)	0.87 (0.15)
CaO	3.57 (0.10)	3.49 (0.21)	3.49 (0.14)	3.42 (0.14)	3.33 (0.14)	3.33 (0.23)	3.36 (0.21)	3.33 (0.31)	3.36 (0.19)
Na_2O	4.47 (0.11)	4.47 (0.44)	4.4 (0.16)	4.14 (0.17)	4.34 (0.07)	4.49 (0.38)	4.54 (0.10)	4.49 (0.13)	4.29 (0.08)
K_2O	2.50 (0.06)	2.57 (0.10)	2.51 (0.07)	2.45 (0.06)	2.56 (0.07)	2.58 (0.17)	2.64 (0.09)	2.62 (0.10)	2.59 (0.06)
P_2O_5	0.18 (0.12)	0.16 (0.13)	0.13 (0.16)	0.19 (0.14)	0.15 (0.14)	0.21 (0.13)	0.19 (0.13)	0.17 (0.11)	0.13 (0.13)
Total	100	100	100	100	100	100	100	100	100

NOTES: Values in parentheses are standard deviations.

Oxide concentrations were recalculated to total 100% by cation balance.

Table 4. Texture of the Sakurajima pumice samples.

Sample	Number of regions	Analyzed area (excluding vesicles)		Px content	Number of crystal cross sections					
		(µm^2)	(vesicle%) [a]	(area%)	All	Oct.	Hept.	Hex.	Pent.	Para.
Type-1	4	1,836,593	75.0	0.01	90	1	1	21	8	30
Type-2	1	106,891	79.8	0.43	559	6	7	190	40	152
Type-3	2	49,054	67.1	2.47	710	264	2	1	0	0

[a] The percentage of vesicles in the analyzed rectangle area.

Table 5. Parameters used in CSDCorrections.

Sample	3D aspect ratio		Roundness	Size scale length
	S:*I*:*L*	*Rc2*		(Bins per decade [a])
Type-1	1:1.40:3.60	0.997	0.5	5
Type-2	1:1.75:6.00	0.984	0.5	
Type-3	1:1.30:4.60	0.999	0.7	

[a] Logarithmic base-10 size scale.

Table 6. Tracht analyses on run products at 955 °C.

Sample		ΔT_{eff} for Px (K)	Analyzed area (μm^2)	Numbers of pyroxene crystals					
Path	P_f (MPa)			Octagon	Heptagon	Hexagon	Pentagon	Parallelogram	Other
EQ	120	~0	6635	115	23	50	5	2	49
SSD	50	35	13614	114	6	3	1	0	36
SSD	20	75	15945	37	18	30	16	33	34
SSD	10	95	23844	13	13	40	22	11	23
SSD	5	110	15905	2	2	13	38	173	31
CD	5	<110	15144	64	9	54	10	4	51

Figure 1

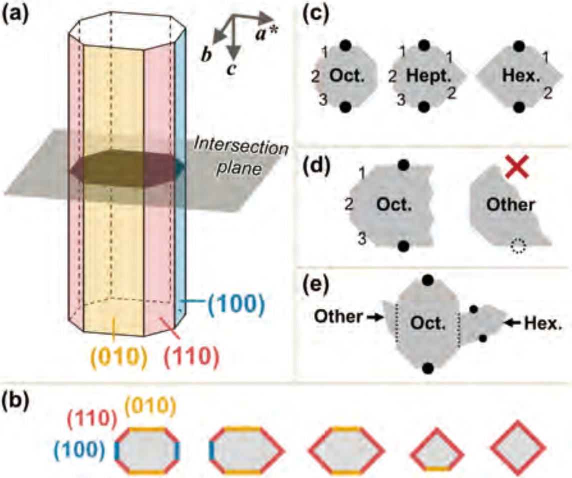

(a)
b
c
a*
Intersection plane
(100)
(010)
(110)
(c)
1
2
3
Oct.
1
1
2
3
2
Hept.
1
2
Hex.
(d)
1
2
3
Oct.
Other
(e)
Other
Oct.
Hex.
(b)
(110)
(010)
(100)

Figure 2

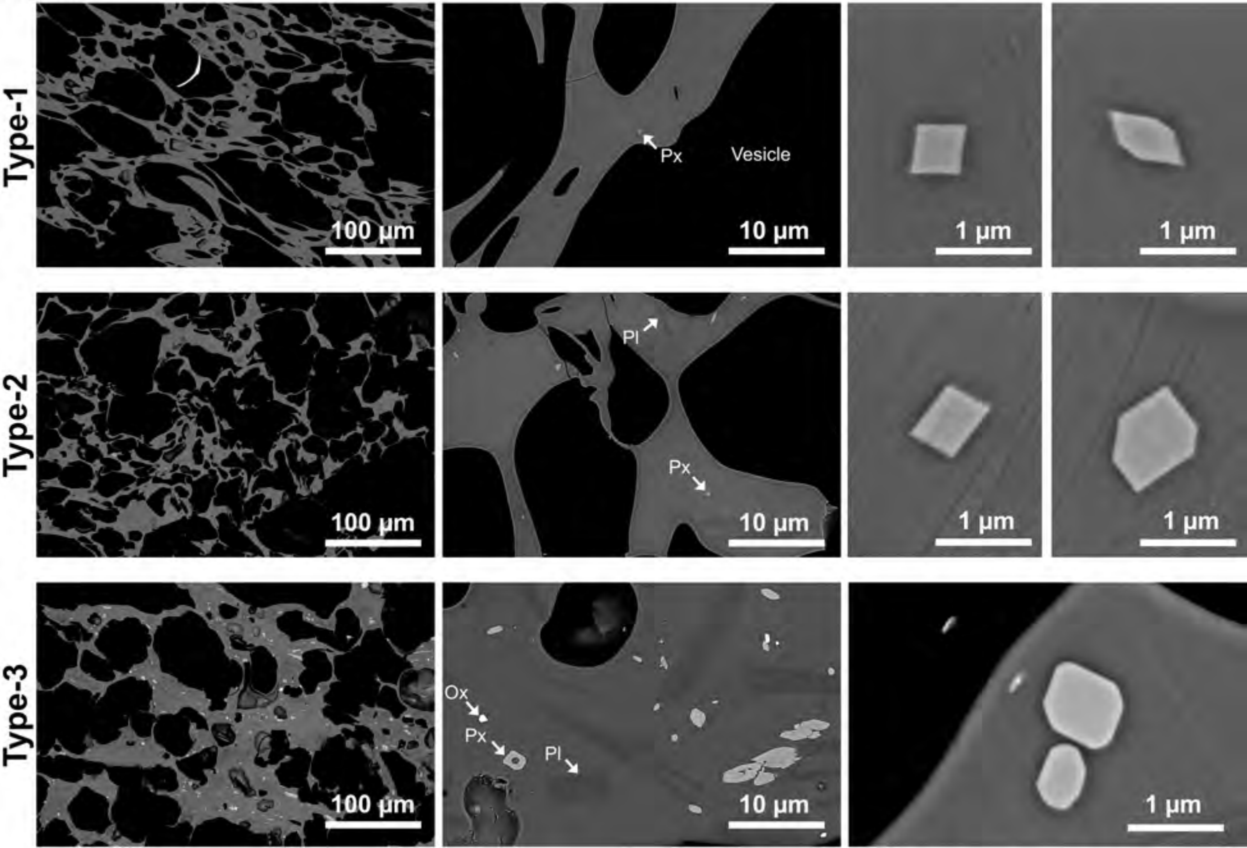
Type-1
100 µm
Px
Vesicle
10 µm
1 µm
1 µm
Type-2
100 µm
Pl
Px
10 µm
1 µm
1 µm
Type-3
100 µm
Ox
Px
Pl
10 µm
1 µm

Figure 3

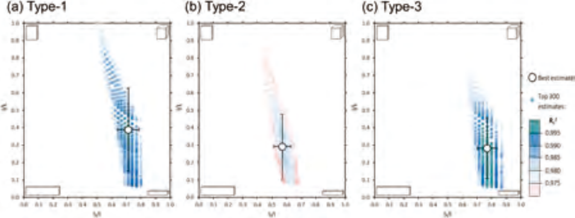

(a) Type-1

(b) Type-2

(c) Type-3

Figure 4

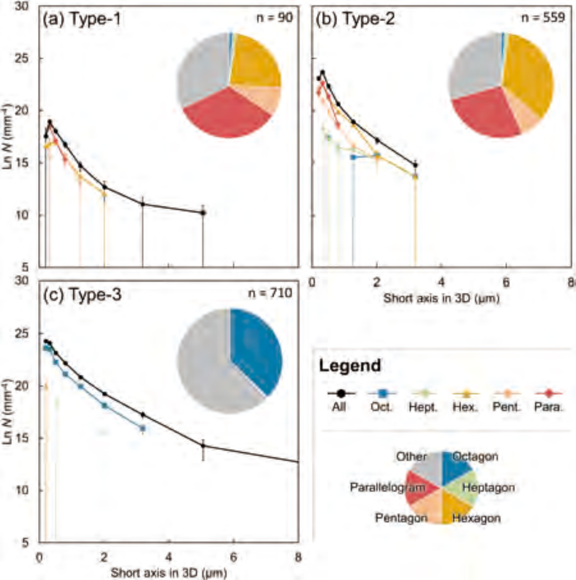

(a) Type-1
n = 90
(b) Type-2
n = 559
(c) Type-3
n = 710
Ln N (mm^{-4})
30
25
20
15
10
5
0
2
4
6
8
Short axis in 3D (μm)
Legend
All
Oct.
Hept.
Hex.
Pent.
Para.
Other
Octagon
Heptagon
Hexagon
Pentagon
Parallelogram

Figure 5

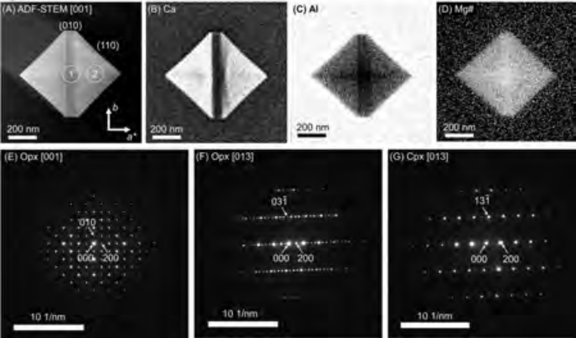
(A) ADF-STEM [001]
(010)
(110)
1
2
200 nm
b
a*
(B) Ca
200 nm
(C) Al
200 nm
(D) Mg#
200 nm
(E) Opx [001]
010
000
200
10 1/nm
(F) Opx [013]
03$\bar{1}$
000
200
10 1/nm
(G) Cpx [013]
13$\bar{1}$
000
200
10 1/nm

Figure 6

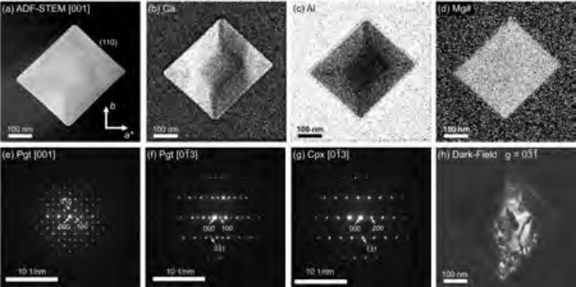
(a) ADF-STEM [001]
(110)
b
a*
100 nm
(b) Ca
100 nm
(c) Al
100 nm
(d) Mg#
100 nm
(e) Pgt [001]
010
000
100
10 1/nm
(f) Pgt [0$\bar{1}$3]
000
100
0$\bar{3}\bar{1}$
10 1/nm
(g) Cpx [0$\bar{1}$3]
000
200
$\bar{1}$31
10 1/nm
(h) Dark-Field g = 03$\bar{1}$
100 nm

Figure 7

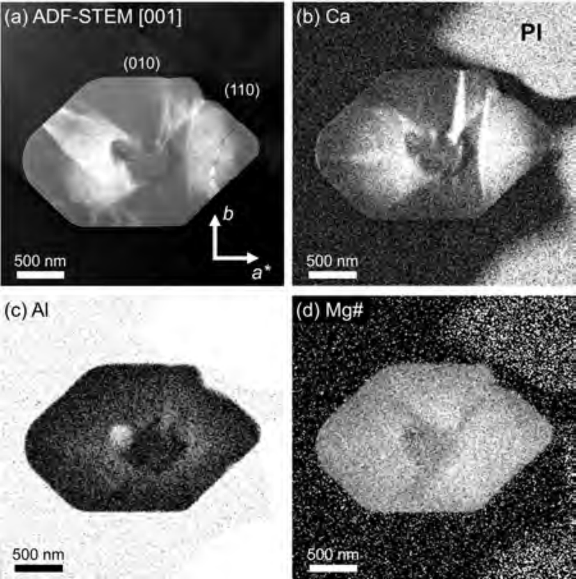
(a) ADF-STEM [001]
(010)
(110)
b
a*
500 nm
(b) Ca
Pl
500 nm
(c) Al
500 nm
(d) Mg#
500 nm

Figure 8

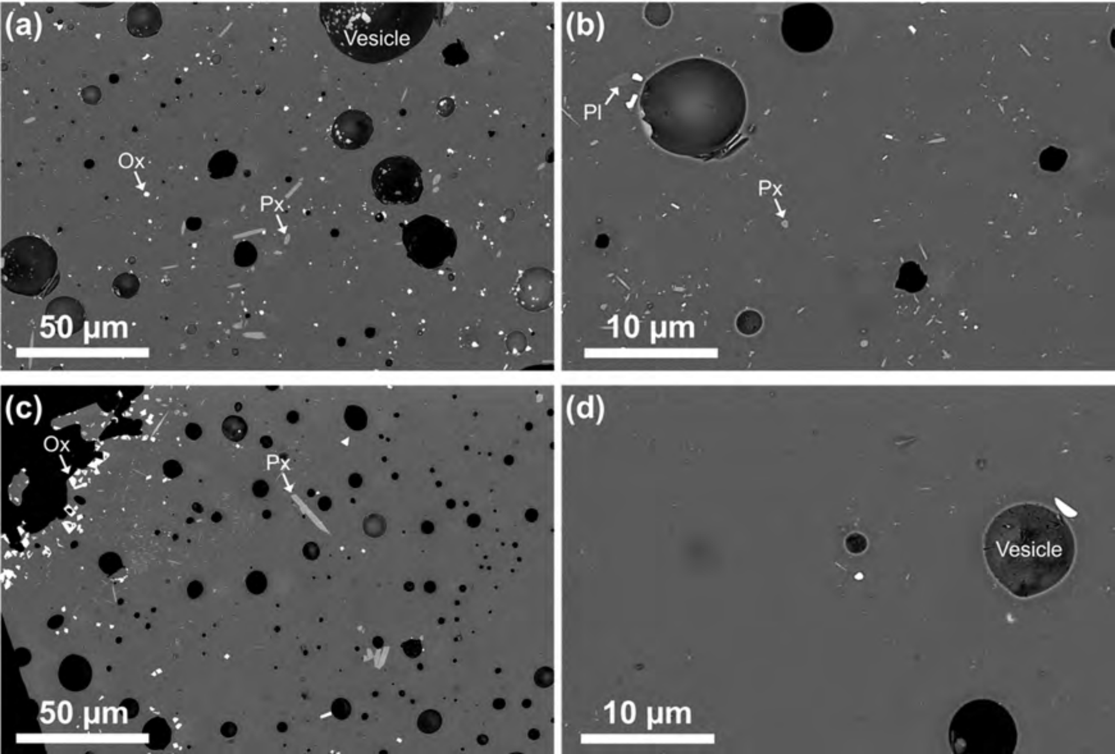

Figure 9

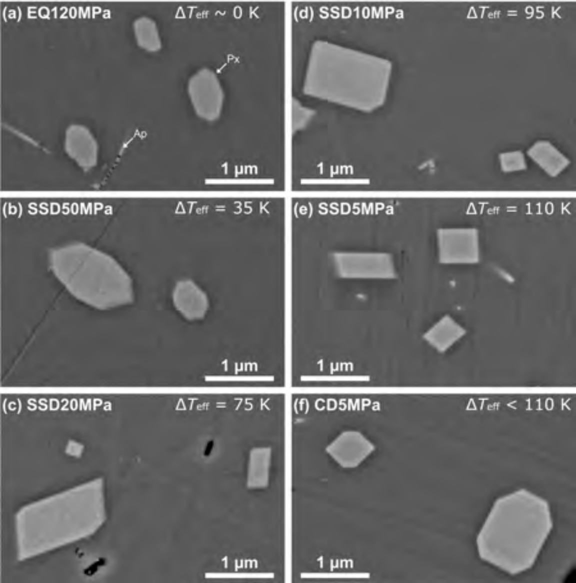

(a) EQ120MPa
ΔTeff ~ 0 K
Px
Ap
1 μm
(d) SSD10MPa
ΔTeff = 95 K
1 μm
(b) SSD50MPa
ΔTeff = 35 K
1 μm
(e) SSD5MPa
ΔTeff = 110 K
1 μm
(c) SSD20MPa
ΔTeff = 75 K
1 μm
(f) CD5MPa
ΔTeff < 110 K
1 μm

Figure 10

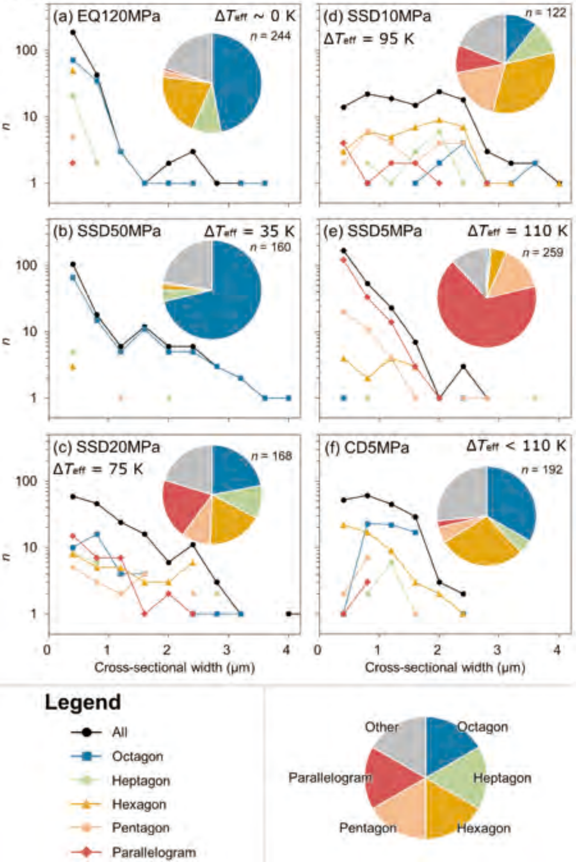
(a) EQ120MPa
ΔTeff ~ 0 K
n = 244
(b) SSD50MPa
ΔTeff = 35 K
n = 160
(c) SSD20MPa
ΔTeff = 75 K
n = 168
(d) SSD10MPa
ΔTeff = 95 K
n = 122
(e) SSD5MPa
ΔTeff = 110 K
n = 259
(f) CD5MPa
ΔTeff < 110 K
n = 192
n
1
10
100
0
1
2
3
4
Cross-sectional width (μm)
Legend
All
Octagon
Heptagon
Hexagon
Pentagon
Parallelogram
Other
Octagon
Heptagon
Hexagon
Pentagon
Parallelogram

Figure 11

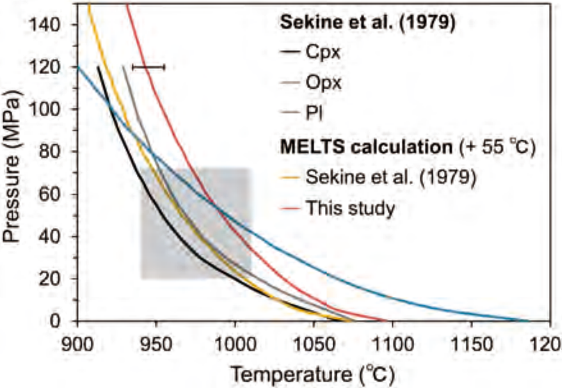
Sekine et al. (1979)
Cpx
Opx
Pl
MELTS calculation (+ 55 °C)
Sekine et al. (1979)
This study
Pressure (MPa)
0
20
40
60
80
100
120
140
Temperature (°C)
900
950
1000
1050
1100
1150
1200

Figure 12

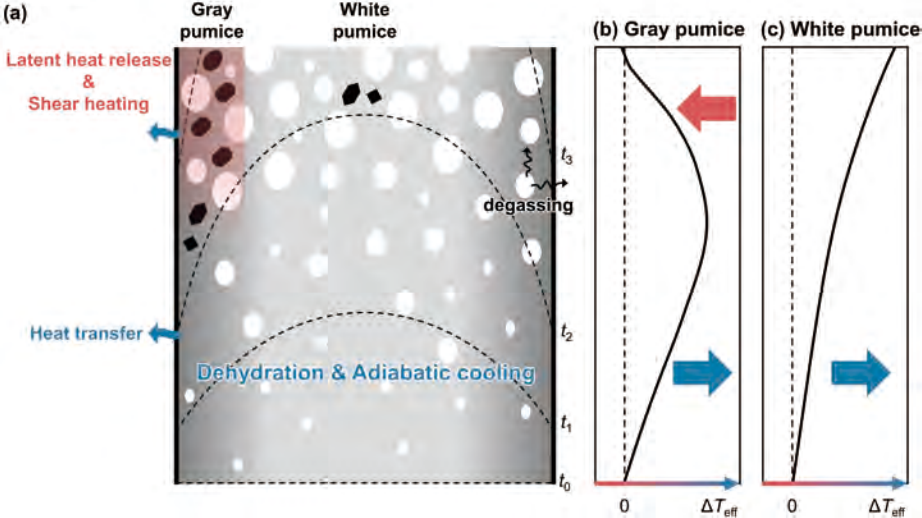
(a)
Gray pumice
White pumice
Latent heat release & Shear heating
Heat transfer
degassing
Dehydration & Adiabatic cooling
t_3
t_2
t_1
t_0
(b) Gray pumice
(c) White pumice
0
ΔT_{eff}
0
ΔT_{eff}